

# Biomimetic Dendrite-Free Multivalent Metal Batteries

Zhijia Zhang, Xu Yang, Peng Li, Yao Wang, Xin Zhao, Javad Safaei, Hao Tian, Dong Zhou,\* Baohua Li,\* Feiyu Kang,\* and Guoxiu Wang\*

Rechargeable multivalent metal (e.g., zinc (Zn) and aluminum (Al)) batteries are ideal choices for large-scale energy storage owing to their intrinsic low cost and safety. However, the poor compatibility between metallic anodes and electrolytes strongly hampers their practical applications. Herein, it is demonstrated that confining multivalent metals in a biomimetic scaffold (Bio-scaffold) can achieve highly efficient multivalent metal plating/stripping. This Bio-scaffold is well-tailored through the synergy of a parallel-aligned array of fractal copper branches and a CaTiO<sub>3</sub> (CTO)-based coating layer. By virtue of this design strategy, the as-developed Bio-scaffold-based Zn- and Al-metal anodes exhibited dendrite-free morphologies with high reversibility and long lifespan, as well as excellent performance for Zn and Al full batteries. Theoretical modeling and experimental investigations reveal that the fractal copper array not only facilitates multivalent ion diffusion and electrolyte wetting but also effectively reduces the local current densities during cycling; Meanwhile, the CTO-based coating layer effectively blocks interfacial side reactions and enables a homogeneous ionic flux. This work opens a new avenue for developing multivalent metal batteries.

meet the ever-growing demand for grid-scale energy storage due to the low reserves and uneven distribution of Li in the earth's crust.<sup>[2]</sup> As alternatives to Li-ion batteries, multivalent metal batteries based on low-cost multivalent metals (e.g., zinc (Zn): 3200 \$ ton<sup>-1</sup>; aluminum (Al): 2300 \$ ton<sup>-1</sup>; whereas Li is as high as 64 000 \$ ton<sup>-1</sup><sup>[3]</sup>) are more economically viable for large-scale stationary energy storage. The multivalent cations (Zn<sup>2+</sup>, Al<sup>3+</sup>, etc.) transfer more than one electron per cation, thus improving the specific energy score of any cells incorporating them.<sup>[4]</sup> Besides, the prevailing non-flammable electrolyte systems (e.g., aqueous<sup>[5]</sup> and ionic liquid<sup>[6]</sup> electrolytes) for multivalent metal batteries can effectively circumvent the safety issues of commercial Li-ion batteries, endowing high reliability during their operation.

Despite the above merits, the research progress on multivalent metal batteries is still far from satisfactory. One of the major challenges is the non-ideal compatibility between metallic anodes and electrolytes.<sup>[7]</sup> Severe interfacial side reactions and corrosions (e.g., the hydrogen (H<sub>2</sub>) evolution and Zn anode corrosion in aqueous Zn batteries;<sup>[8]</sup> the strong corrosivity of high-acidity and/or high-chloride-concentration ionic liquid electrolytes toward battery components in the Al batteries<sup>[9]</sup>) remarkably reduce the reversibility and cyclability of such batteries. Moreover, due to the inhomogeneous electric field distribution at surface defects, uncontrollable dendrite growth occurs on multivalent metal surfaces. This issue not only triggers huge safety concerns but also dramatically enlarges the anode surface area to aggravate interfacial side reactions (Figure 1a).<sup>[10]</sup> All these drawbacks have greatly hampered the development of multivalent metal batteries.

Many approaches have been developed to solve the above issues. Although electrolyte engineering (e.g., introducing additives<sup>[11]</sup> and developing water-in-salt<sup>[12]</sup> or gel<sup>[13]</sup> electrolytes) and anode surface coating (e.g., constructing interfacial layers based on polymers,<sup>[14]</sup> metal-organic frameworks,<sup>[15]</sup> or oxides<sup>[16]</sup>) can optimize the interface chemical environment and thus improve the compatibility between multivalent metal anodes and electrolytes, a rational interfacial modification at the atomic level remains a challenge. Other efforts have been focused on confining multivalent metals into carbonaceous,<sup>[17]</sup> nanosheet-stacked,<sup>[18]</sup> and porous-metal<sup>[19]</sup> 3D scaffolds, which are expected to decrease local current density and suppress dendrite growth.<sup>[20]</sup> Nevertheless, most 3D scaffolds possess high tortuosity, which inevitably prolongs the ion-transport length

## 1. Introduction

Energy storage is critical for the integration of renewable energies and the electrification of road transport. Lithium (Li)-ion batteries have dominated the markets of electric vehicles and electrical energy storage.<sup>[1]</sup> However, Li-ion batteries cannot

Z. Zhang, Y. Wang, X. Zhao, D. Zhou, B. Li, F. Kang  
Tsinghua Shenzhen International Graduate School  
Tsinghua University  
Shenzhen 518055, P. R. China  
E-mail: zhou.d@sz.tsinghua.edu.cn; libh@mail.sz.tsinghua.edu.cn;  
fykang@tsinghua.edu.cn

Z. Zhang, X. Yang, J. Safaei, H. Tian, G. Wang  
Centre for Clean Energy Technology  
Faculty of Science  
University of Technology Sydney  
Sydney, NSW 2007, Australia  
E-mail: guoxiu.wang@uts.edu.au

P. Li  
College of Material Science and Engineering  
Nanjing University of Aeronautics and Astronautics  
Nanjing 210006, P. R. China

 The ORCID identification number(s) for the author(s) of this article can be found under <https://doi.org/10.1002/adma.202206970>.

© 2022 The Authors. Advanced Materials published by Wiley-VCH GmbH. This is an open access article under the terms of the Creative Commons Attribution License, which permits use, distribution and reproduction in any medium, provided the original work is properly cited.

DOI: 10.1002/adma.202206970

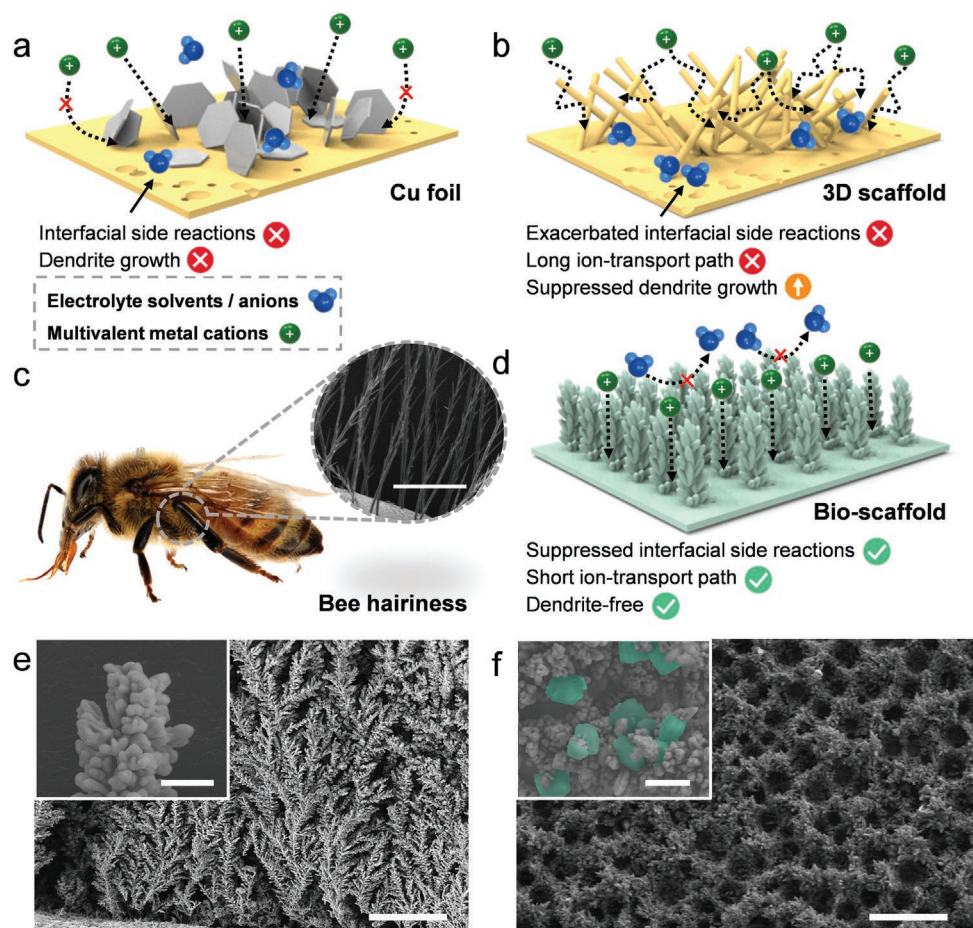


**Figure 1.** Schematic illustration and material characterizations of the Bio-scaffold. a,b) Schematic illustrations of the multivalent metal plating/stripping process on pristine Cu foil (a) and 3D scaffold (b). c) Optical image of a pinned honeybee. Adapted under the terms of the CC-BY Creative Commons Attribution 4.0 International license (<https://creativecommons.org/licenses/by/4.0/>).<sup>[22]</sup> Copyright 2022, The Authors, published by MDPI. An SEM image of bee hairiness is shown in the inset. d) Schematic illustration of the multivalent metal plating/stripping process on the Bio-scaffold. e) Cross-sectional SEM image of a 3D fractal Cu array and its Cu branch magnified (inset). f) Top-view SEM images of a Bio-scaffold. The CTO particles are dyed with malachite green in the magnified region shown in the inset. Scale bars: 100  $\mu\text{m}$  in the inset of (c); 30  $\mu\text{m}$  in (e); 2  $\mu\text{m}$  in the inset of (e); 250  $\mu\text{m}$  in (f); and 5  $\mu\text{m}$  in the inset of (f).

and causes preferential deposition of multivalent metals on the outer electrode surface.<sup>[21]</sup> Moreover, the excessive interfacial area between anodes and electrolytes, originating from the use of previous 3D scaffolding approaches, has exacerbated the unwanted interfacial side reactions (Figure 1b).

During billion of years of evolution, nature has developed numerous perfect biosystems. To facilitate pollen collection, the leg and body hairs of honey bees are aligned approximately parallel to each other, and possess a natural fractal secondary structure with a large surface area, thus enabling massive pollen loading (Figure 1c).<sup>[22]</sup> Inspired by this nanoarchitecture, herein for the first time, we present a biomimetic scaffold (Bio-scaffold) as a multivalent metal host to control the interfacial behavior and suppress dendritic growth. This Bio-scaffold is composed of a parallelly aligned array of fractal copper (Cu) branches, which are coated by a  $\text{CaTiO}_3$  (CTO)-based protective layer. The parallel array structure of the Bio-scaffold effectively shortens the vertical ionic-transport distance to support the fast kinetics of multivalent metal plating/stripping. Meanwhile, the oriented fractal Cu branches in the Bio-scaffold not only

enable superhydrophilicity to facilitate electrolyte wetting but also efficiently reduce local current densities to block dendrite formation. Furthermore, the CTO-based coating layer significantly blocks interfacial side reactions and corrosion. More importantly, the scaffold simultaneously possesses high dielectric constants to further regulate the flux of multivalent metal ions and high multivalent metal-philic characteristics to initiate multivalent metal nucleation inside the scaffold, thus endowing a dendrite-free multivalent metal plating/stripping with high Coulombic efficiency (CE, Figure 1d). As demonstration models, we show that the well-tailored Bio-scaffold exhibited high CEs (99.83% and 99.81% for Zn and Al cells, respectively), low overpotentials, and long lifespans (4000 cycles at 5  $\text{mA cm}^{-2}$  and 1 500 cycles at 1  $\text{mA cm}^{-2}$  for Zn and Al cells, respectively) during repeated Zn and Al plating/stripping processes without dendrite formation. When applied in  $\text{Zn}||\text{V}_{10}\text{O}_{24}\cdot 12\text{H}_2\text{O}$  (VOH) and  $\text{Al}||\text{graphite}$  batteries, the as-developed Bio-scaffold-based full cells delivered enhanced specific capacities and extended cyclability compared with cells using traditional multivalent metal anodes.

## 2. Results and Discussion

To construct a scaffold enabling fast multivalent metal ion diffusion and low local current density, a vertically aligned 3D fractal Cu array was facilely synthesized via aqueous electrodeposition (Figure S1, Supporting Information). As seen from the scanning electron microscopy (SEM) images in Figure 1e, the Cu branch with a diameter of  $\approx 2 \mu\text{m}$  in the 3D array exhibited a typical fractal architecture with both micro- and nanoscale features. The surface of the 3D Cu array depicted a highly ordered porous structure (Figure S2a,b, Supporting Information), which facilitated electrolyte wetting and ion transport. To suppress interfacial side reactions, the Bio-scaffold was obtained after uniformly coating the 3D Cu array with ultrathin protective polyacrylonitrile (PAN) layer with a thickness of  $\approx 10 \text{ nm}$  (Figure S2c,d, Supporting Information). CTO particles with an average diameter of  $\approx 2 \mu\text{m}$  were evenly dispersed on the PAN layer (the inset of Figure 1f; Figure S3, Supporting Information), efficiently regulating the nucleation and plating of multivalent metals. It is noted that the fractal structure of the Cu branch was well-maintained (Figure S2c, Supporting Information; Figure 1f) after surface coating of the CTO-based layer (see the X-ray diffraction (XRD) and Fourier-transform infrared (FT-IR) spectroscopy results in Figure S4, Supporting Information). Such a rationally designed Bio-scaffold was expected to endow dendrite-free multivalent metal plating/stripping without noticeable interfacial side reactions.

The as-prepared Bio-scaffold was applied in aqueous Zn-ion batteries. It is known that the wettability of electrodes with

aqueous electrolytes played a key role in the electrode|electrolyte interfacial contact, which can be quantitatively evaluated for contact angle analysis. Based on the Wenzel model, the wetting behavior on rough surfaces can be described as Equation (1)<sup>[23]</sup>

$$\cos \theta = R \frac{\gamma_{sv} - \gamma_{sl}}{\gamma_{lv}} \quad (1)$$

where  $\theta$  is the measured contact angle;  $R$  is the roughness of the actual surface;  $\gamma_{sv}$ ,  $\gamma_{sl}$ , and  $\gamma_{lv}$  are the solid|vapor, solid|liquid, and liquid|vapor surface tensions, respectively. Therefore, increasing the roughness of the hydrophilic electrode surface can improve the aqueous electrolyte wettability of the electrode.<sup>[24]</sup> As shown in the upper panel of Figure 2a, a flat Cu foil exhibited weak hydrophilicity with a water contact angle of  $60^\circ$ . As expected, the water contact angle of the 3D fractal Cu array dropped sharply to  $0^\circ$ , demonstrating a superhydrophilicity originating from the ultrahigh roughness of the 3D fractal Cu array (Figure 2a, the middle panel). This superhydrophilic property can be well-maintained after the coating of a high-polarity CTO-based layer (Figure 2a, the lower panel), ensuring an excellent affinity for aqueous electrolytes to endow their complete absorption into the Bio-scaffold.

As an irreversible decomposition behavior of aqueous electrolytes, the hydrogen evolution reaction (HER) on the anode surface parasitizes the Zn deposition process, strongly deteriorating the CE and cyclability of aqueous batteries.<sup>[25]</sup> We evaluated the HER on different electrode surfaces in  $1 \text{ M Na}_2\text{SO}_4$  aqueous electrolyte by linear sweep voltammetry (LSV). Na salts were used to exclude the influence of the competitive Zn

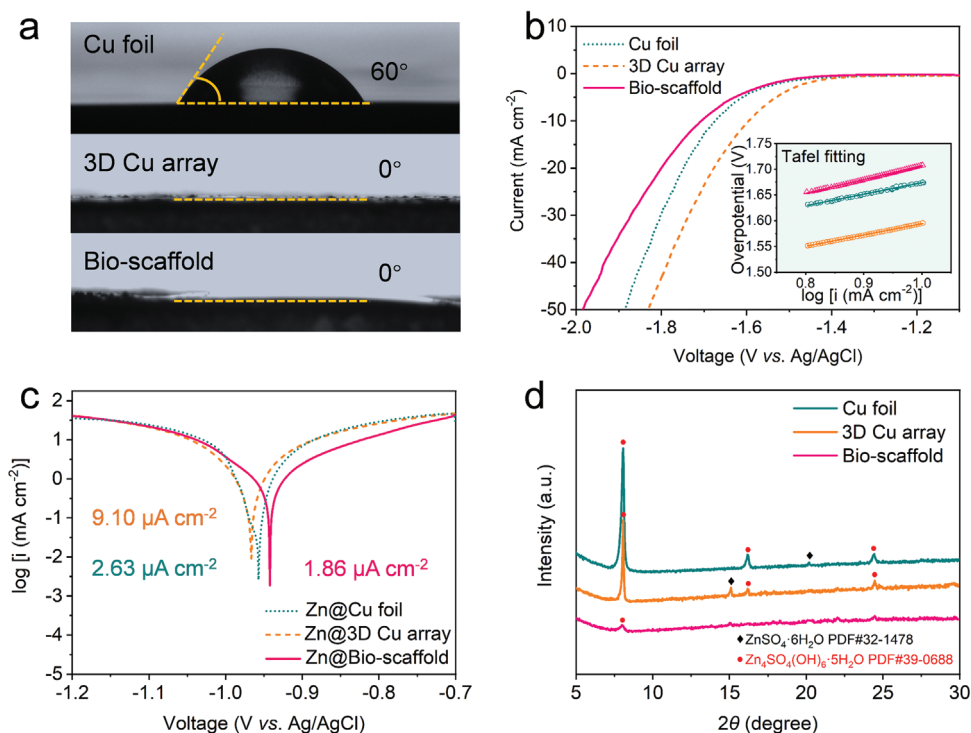


**Figure 2.** Compatibility between Zn@Bio-scaffold and aqueous electrolytes. a) Static contact angles of water on Cu foil, 3D Cu array, and Bio-scaffold. b) LSV curves recorded at  $1 \text{ mV s}^{-1}$  and corresponding Tafel plots (inset) of different electrodes in the presence of  $1 \text{ M Na}_2\text{SO}_4$  aqueous electrolyte. c) LSV curves of different electrodes in  $2 \text{ M ZnSO}_4$  aqueous electrolyte at  $1 \text{ mV s}^{-1}$ . d) XRD patterns of different substrates after the first Zn plating/stripping cycle at  $1 \text{ mA cm}^{-2}$  and an areal capacity of  $1 \text{ mAh cm}^{-2}$ .

plating process rather than Zn salts.<sup>[26]</sup> Compared with pristine Cu foil—the onset potential for HER on 3D Cu arrays significantly decreased from  $-1.67$  to  $-1.59$  V (Figure 2b) accompanied by a decrease of Tafel slope (from  $223$  mV dec<sup>-1</sup> to  $212$  mV dec<sup>-1</sup>, see inset of Figure 2b). This positive shift of HER was mainly caused by the excess surface area of the fractal Cu array that exacerbated electrolyte decomposition. In contrast, the Bio-scaffold exhibited a largely negative shift for HER onset potential (i.e.,  $-1.71$  V, Figure 2b); meanwhile, the Tafel slope ( $246$  mV dec<sup>-1</sup>) of the Bio-scaffold was higher than that of pristine Cu foil (the inset of Figure 2b). This implies that the electron-insulated CTO-based coating layer acts as an effective barrier against the interfacial decomposition of aqueous electrolytes on the electrodes. High resistance to self-corrosion is required to ensure the stability of Zn-metal batteries in aqueous electrolytes.<sup>[27]</sup> We prepared Zn@Cu foil, Zn@3D Cu array, and Zn@Bio-scaffold electrodes via electrodeposition process (Figure S5, Supporting Information). The Zn@Bio-scaffold electrode delivered a corrosion onset voltage of  $-0.942$  V, much higher than those of Zn@Cu foil ( $-0.957$  V) and Zn@3D Cu array ( $-0.967$  V), suggesting a superior anti-corrosion ability (Figure 2c). The corrosion current of Zn@Bio-scaffold was as low as  $1.86$  mA cm<sup>-2</sup>, reflecting sluggish corrosion kinetics. XRD measurements can further corroborate this result. For the Bio-scaffold after the first Zn plating/stripping cycle, the peak intensities of Zn<sub>4</sub>SO<sub>4</sub>(OH)<sub>6</sub>·5H<sub>2</sub>O (PDF #39-0688) as the interfacial side reaction products were negligible compared with those of the cycled Cu-foil and 3D Cu array electrodes (Figure 2d).<sup>[28]</sup> This is mainly attributed to the fact that the CTO-based coating layer with a high dielectric constant can repel electrolyte solvent molecules and anions by the synergistic effect of physical shielding and dipole interactions,<sup>[29]</sup> thus dramatically improving the compatibility between Zn electrode and aqueous electrolytes.

The effect of the Bio-scaffold on the morphology evolution during the Zn plating process was monitored in situ on transparent Zn||Cu asymmetric cells under a current density of  $5$  mA cm<sup>-2</sup>. As shown in the left panels of Figure 3a, the Zn deposition layer became highly porous with massive dendrites on the Cu foil after plating for 90 min. Although the dendrite growth was remarkably suppressed, gas bubbles appeared on the 3D Cu array surface, implying a severe HER originated from the high electrolyte contact area of the 3D Cu array (Figure S6, Supporting Information). On the contrary, the Bio-scaffold exhibited a dense deposition morphology with no dendritic structures or gas bubbles during the 90 min plating (the right panels of Figure 3a; Figure S6, Supporting Information). Such unique plating behavior on the Bio-scaffold was validated by chronoamperometry (CA) tests in symmetrical cells (Figure S7, Supporting Information). Zn ions tended to undergo a frantic planar diffusion process (i.e., 2D diffusion, as seen from the continuous current increase during the initial CA process) on the Cu foil, which triggered nonuniform Zn plating and dendrite formation.<sup>[30]</sup> By comparison, the Bio-scaffold showed a steady polarization current throughout the CA process, indicating a stable 3D diffusion behavior that facilitated homogeneous and dendrite-free Zn plating.

Density functional theory (DFT) calculations were conducted to further investigate the interaction between Zn atoms and different substrates. The binding energy of a Zn atom absorbed on the CTO (121) plane was calculated to be  $-4.2$  eV (Figure 3b, right panel), much higher than those absorbed on Zn (002) plane ( $-0.61$  eV, Figure S8, Supporting Information) and Cu (111) plane ( $-1.1$  eV, Figure 3b, left panel) substrates, verifying that Zn atoms prefer to nucleate on the CTO particles rather than Cu or Zn substrates in the Bio-scaffold. This high Zn-philicity of CTO promotes preferential nucleation of Zn metal during plating, making CTO particles an ideal “seed point” for

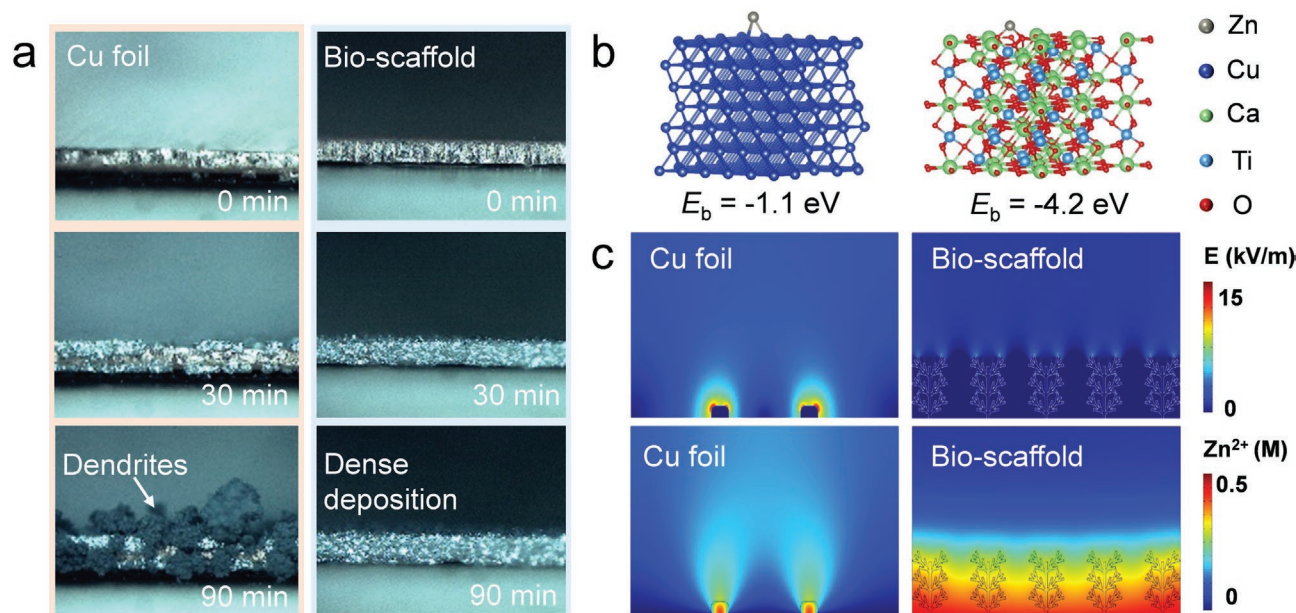


**Figure 3.** Zn-plating experiment and corresponding computations on the Bio-scaffold. a) In situ optical microscopy visualization of Zn deposited on Cu foil (left) and Bio-scaffold (right) under a current density of  $5$  mA cm<sup>-2</sup>. b) DFT-calculated binding energies of Zn atoms with Cu (left) and CTO (right). c) Numerical simulations of electric field distributions (top) and ion concentration fields (bottom) on Cu foil (left) and Bio-scaffold (right).

the development of a dendrite-free Zn-metal anode. Numerical simulation of the Zn deposition process on different substrates was conducted using the COMSOL program with a nuclei size of  $1\ \mu\text{m}$  and an overpotential of  $1\ \text{V}$  for  $1\ \text{s}$ . Uneven electric field (Figure 3c, the upper left panel) accumulated on the tops of Zn nuclei was observed on the Cu foil. Zn ions were preferentially deposited at these “hot spots”,<sup>[31]</sup> giving rise to inhomogeneous  $\text{Zn}^{2+}$  concentration distribution (Figure 3c, lower left panel) and growth. Owing to the enlarged surface area of the 3D fractal array structure, the electric field and Zn ion flux were distributed much more homogeneously on the 3D Cu arrays (Figure S9, Supporting Information). Moreover, as expected, the high dielectric constant of CTO ( $\epsilon_{\text{max}}$ :  $331$ )<sup>[32]</sup> in the Bio-scaffold promoted a rapid Zn ion diffusion to the bottom of the scaffold, meanwhile, the concentration of  $\text{Zn}^{2+}$  (Figure 3c,

the lower right panel) was further homogenized. Such a synergistic effect of the 3D fractal array structure and CTO-based coating layer efficiently stabilizes the Zn electrodeposition and contributes to the dendrite-free Zn-plating morphologies in Figure 3a.

$\text{Zn@Bio-scaffold}||\text{Zn@Bio-scaffold}$  symmetric cells were assembled to further measure the long-term galvanostatic cycling performance at  $1\ \text{mA cm}^{-2}$ . Symmetric cells with two Zn@Cu foil or Zn@3D Cu array electrodes were also assembled for comparison. The Zn@Cu foil||Zn@Cu foil cell delivered a voltage hysteresis of  $\approx 39\ \text{mV}$ , which suddenly dropped to  $\approx 0\ \text{V}$  at the 404th hour, indicating a short-circuit induced by dendrite growth (Figure 4a).<sup>[33]</sup> The Zn@3D Cu array||Zn@3D Cu array cell showed an average overpotential of  $\approx 29\ \text{mV}$ , meanwhile, the overpotential increased sharply at

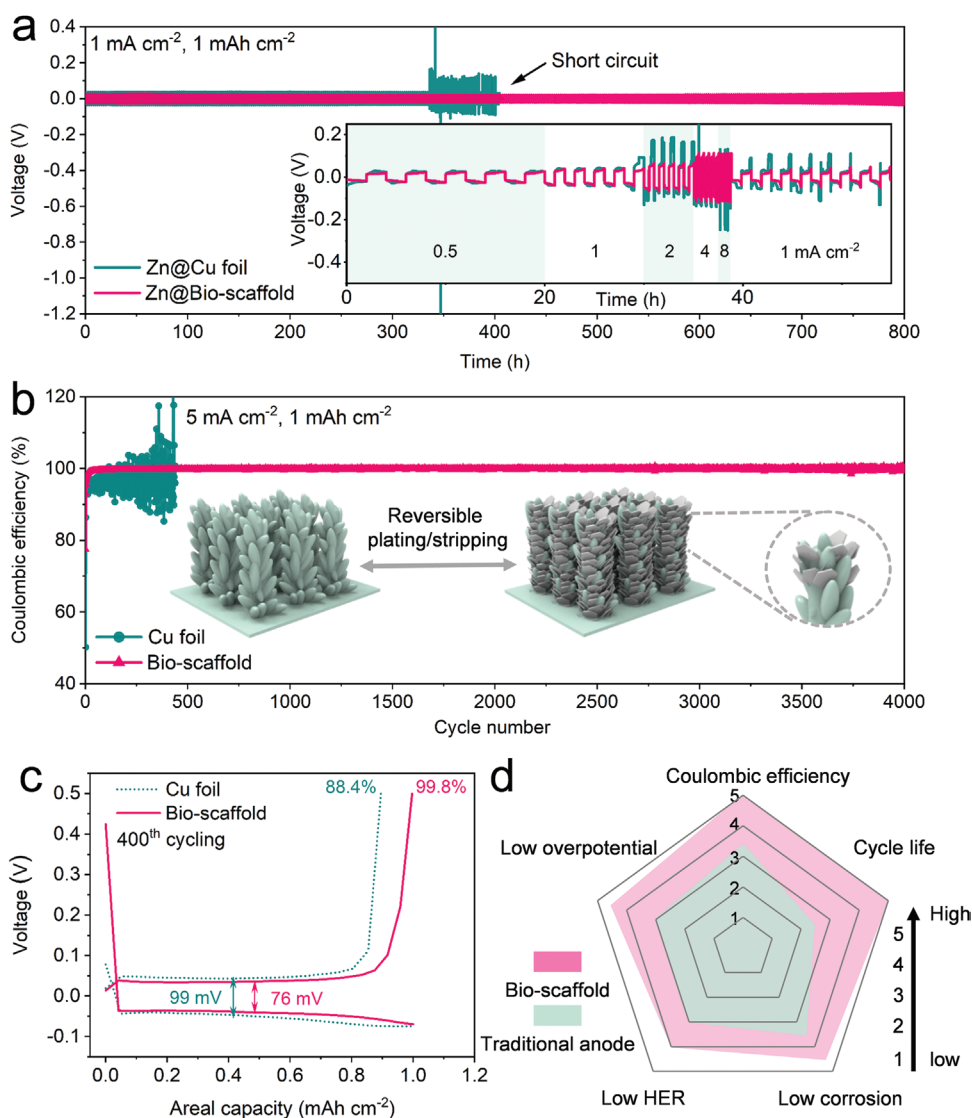


**Figure 4.** Electrochemical performance of Bio-scaffold. a) Voltage profiles of symmetric cells with Zn@Cu foil or Zn@Bio-scaffold electrodes at  $1\ \text{mA cm}^{-2}$  with a capacity of  $1\ \text{mAh cm}^{-2}$ . The rate performance of the two symmetric cells at different current densities is shown in the inset. b) CEs of Zn plating/stripping on Cu foil and Bio-scaffold at  $5\ \text{mA cm}^{-2}$  with a capacity of  $1\ \text{mAh cm}^{-2}$ . A schematic illustration of the reversible Zn plating/stripping behavior on the Bio-scaffold is shown in the inset. c) Corresponding voltage profiles of Zn||Cu foil and Zn||Bio-scaffold cells at the 400th cycle. d) Performance comparisons of reported Zn-metal scaffolds/current collectors and our Bio-scaffold based on five parameters.

the 342nd hour due to the uncontrolled interfacial side reactions (Figure S10, Supporting Information). In contrast, the Zn@Bio-scaffold||Zn@Bio-scaffold cell delivered a flat voltage plateau during Zn plating and stripping processes with a reduced voltage hysteresis of  $\approx 26$  mV, which maintained steady without a noticeable during 800 h cycling (Figure 4a). Additionally, the Zn@Bio-scaffold electrode also delivered superior rate performance. The symmetric cell with Zn@Bio-scaffold electrode displayed voltage hysteresis of 14, 26, 51, 92, and 109 mV when current densities were increased from  $0.5 \text{ mA cm}^{-2}$  to  $8 \text{ mA cm}^{-2}$ , respectively, being much lower than those of Zn@Cu foil||Zn@Cu foil cell (inset of Figure 4a). This result implies that the parallel array structure of the Bio-scaffold efficiently shortens the ionic-transport distance and reduces the local current density, endowing fast Zn ion diffusion and regulating the Zn-metal deposition at high current densities.

The reversibility of Zn plating/stripping on different substrates was further investigated using asymmetric cells. The Cu foil exhibited low CEs (CEs  $\approx 96.88\%$  and  $96.92\%$  at 1 and  $5 \text{ mA cm}^{-2}$ , respectively) and short lifespans (136 and 358 cycles at 1 and  $5 \text{ mA cm}^{-2}$ , respectively), which can be attributed to the growth of dendritic Zn and severe interfacial side reactions (Figure 4b; Figure S11, Supporting Information). The 3D Cu array scaffold delivered improved average CEs of  $98.13\%$  and  $98.86\%$  at 1 and  $5 \text{ mA cm}^{-2}$  during the cycling process, respectively, which could be ascribed to the high scaffold surface area derived from significantly reduced local current densities (Figure S11, Supporting Information). However, the cells with the 3D Cu array scaffolds still suffered from limited cycling life, with CE dropping significantly beyond 306 cycles at  $1 \text{ mA cm}^{-2}$  and 500 cycles at  $5 \text{ mA cm}^{-2}$ , respectively. Noticeably, the Bio-scaffold achieved much higher average CEs ( $\approx 98.77\%$  and  $99.83\%$  at 1 and  $5 \text{ mA cm}^{-2}$ , respectively) and cyclability (500 and 4000 cycles at 1 and  $5 \text{ mA cm}^{-2}$ , respectively; Figure 4b; Figure S11, Supporting Information), indicating a highly reversible Zn plating/stripping behavior. The current density plays a contradictory role in the CE of metal plating/stripping. The kinetics of dendrite growth speeds up at high current densities, increasing the electrode surface area and thus reducing the CE.<sup>[10]</sup> However, interfacial side reactions such as electrolyte decomposition are less severe at high current densities.<sup>[34]</sup> Besides, the nucleation overpotential and nucleation sites increase under high current densities, promoting a uniform plating of the multivalent metal. Therefore, the Zn||Cu cells showed better cycle stability and high CEs under higher current densities. The corresponding voltage profiles for Zn plating/stripping on different substrates are shown in Figure 4c and Figure S12 (Supporting Information). The Bio-scaffold exhibited a smaller voltage gap between charge and discharge plateaus ( $\approx 76$  mV, Figure 4c) at the 400th cycle compared with those of Cu foil ( $\approx 99$  mV, Figure 4c) and plain 3D Cu arrays (81 mV, Figure S12, Supporting Information), suggesting a reduced polarization ascribed to the homogeneous Zn plating/stripping and suppressed interfacial side reactions of the Bio-scaffold. The voltage hysteresis and CEs of Zn||Cu cells at a high plating/stripping capacity of  $5 \text{ mAh cm}^{-2}$  have been measured, and the results are shown in Figure S13 (Supporting Information). It can be seen that the Zn||Bio-scaffold cell showed smaller voltage hysteresis (62 mV, Figure S13a,

Supporting Information) than the Zn||Cu foil and Zn||3D Cu array cells. It maintained a high CE of  $99.6\%$  after 50 cycles (Figure S13b, Supporting Information), while the Zn||Cu foil and Zn||3D Cu array cells suffered from battery failure in 11 and 25 cycles, respectively. This superior electrochemical performance of Bio-scaffold under higher plating/stripping capacities benefits the real-world application in batteries with high active material areal mass loadings. The performances of previously reported Zn-metal scaffolds/current collectors and our Bio-scaffold were compared in terms of five aspects. As schematically shown in Figure 4e based on the data in Table S1 (Supporting Information), to the best of our knowledge, our Bio-scaffold presented attractive merits over Zn anode and other counterparts including high CE, long cycle CE life, limited corrosion, and HER, and low overpotential in plating/stripping processes. All of these validate the great application viability of Bio-scaffold in practical multivalent metal batteries.

Morphological evolutions of Zn plating/stripping on different substrates were investigated by ex situ SEM with deposition capacities up to  $1 \text{ mAh cm}^{-2}$  followed by complete stripping at  $1 \text{ mA cm}^{-2}$ . As seen from the upper panels in Figure S15 (Supporting Information), the smooth surface of the Cu foil significantly altered to form a pulverized and by-product stacking morphology with increasing deposition capacities. Massive Zn dendrites and dead Zn remained on the Cu foil after the stripping process, giving rise to the low CE in Figure S11 (Supporting Information). In contrast, the morphological evolutions of Zn plating/stripping on the 3D Cu array (the middle panels in Figure S15, Supporting Information) and Bio-scaffold (the lower panels in Figure S15, Supporting Information) were highly reversible. Hexagonal Zn pieces were uniformly plated inside the voids between the fractal branches of the Bio-scaffold, meanwhile the fractal branches maintained their structural integrity well after the stripping process without residual dead Zn or by-products. Such high Zn plating/stripping reversibility of Bio-scaffold endows assembled cells with high CE and long lifespan (Figure S11, Supporting Information; Figure 4b, inset).

As a proof of concept, Zn full cells were assembled using the Zn@Bio-scaffold prepared by electrodeposition as anode and layered VOH as the cathode (Figure S16, Supporting Information). Cycling voltammetry (CV) tests were carried out between  $0.5\text{--}1.5$  V at a scan rate of  $0.1 \text{ mV s}^{-1}$ . As shown in Figure 5a, three redox peaks,  $0.62/0.78$ ,  $0.97/1.07$ , and  $1.3/1.33$  V, appeared in the 2nd CV curve of the Zn||VOH full cells, implying a multistep  $\text{Zn}^{2+}/\text{H}^+$  co-insertion/deintercalation process.<sup>[35]</sup> The higher peak current densities and the lower potential gap between the main anodic and cathodic peaks of the Zn@Bio-scaffold||VOH cell compared with other counterparts indicated the fast kinetics of Zn plating/stripping on the Zn@Bio-scaffold (Figure 5a; Figure S17a, Supporting Information), which can be further verified by the Galvanostatic intermittent titration technique (GITT). As seen from the magnified region of the GITT curves in the inset of Figure 5b,  $\Delta E_t$  is the potential change during the constant current pulse excluding the IR drop,  $IR_1$  and  $IR_2$  are the voltage drops during the end or the beginning of pulse current, respectively.<sup>[36]</sup> As expected, the overpotential of VOH-based cells using Zn@Bio-scaffold anodes was much lower than that using Zn@Cu foil anodes

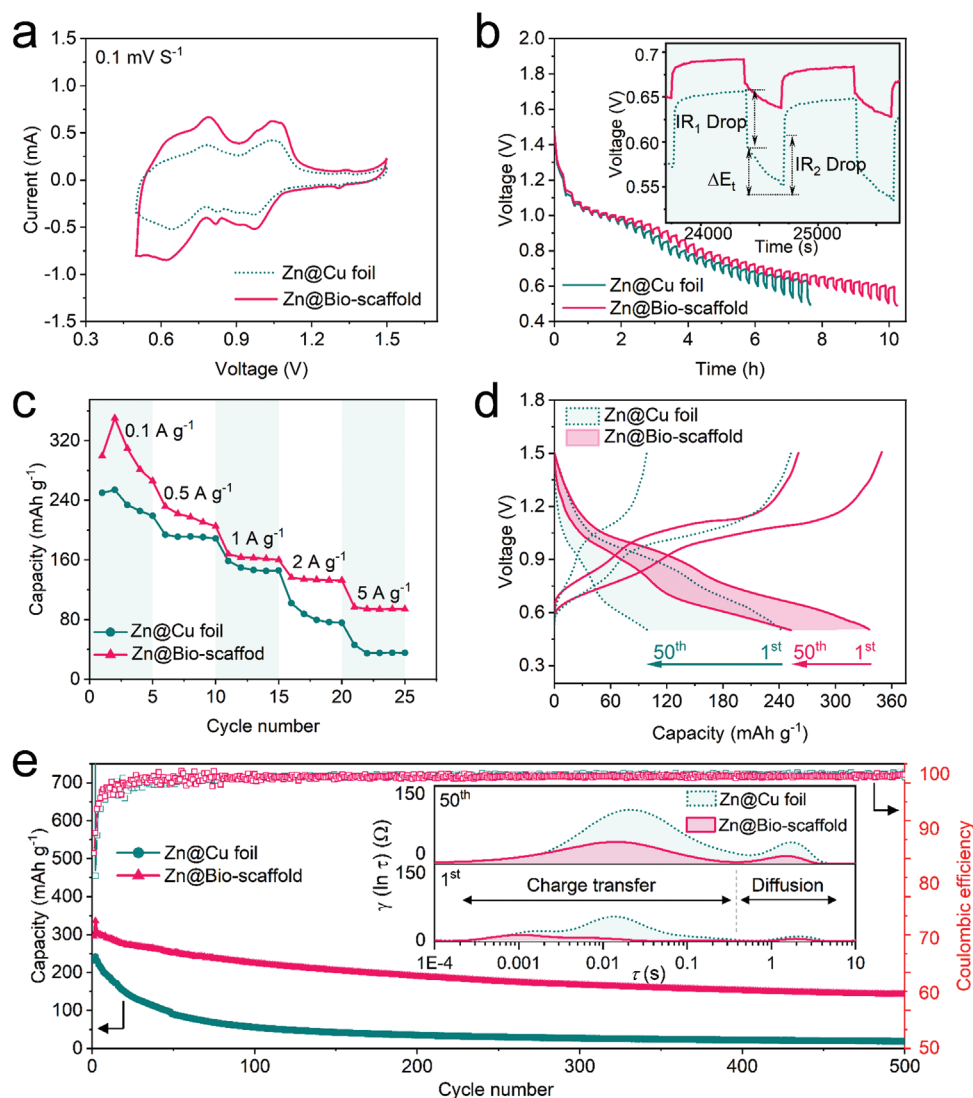


**Figure 5.** Electrochemical performance of Zn@Bio-scaffold||VOH full batteries. a) CV curves at  $0.1 \text{ mV s}^{-1}$ , b) GITT profiles, and c) rate performance of the Zn@Cu||VOH and Zn@Bio-scaffold||VOH cells. d) The 1st and 50th discharge–charge profiles and e) cycling performance of the Zn@Cu||VOH and Zn@Bio-scaffold||VOH cells at a current density of  $2 \text{ A g}^{-1}$ . The corresponding DRT profiles of the cells after 1 cycle and 50 cycles are shown in the inset.

(Figure 5b), validating a low ohmic polarization attributed to the fast ion diffusion through the Bio-scaffold and the elimination of by-products on the anode surface.

Figure 5c and Figure S17b (Supporting Information), show the rate performance of VOH-based Zn cells. The Zn@Bio-scaffold||VOH cell achieved high capacities of 309, 221, 163, 134, and  $94 \text{ mAh g}^{-1}$  (based on the mass of VOH) at 0.1, 0.5, 1, 2,  $5 \text{ A g}^{-1}$ , respectively (Figure 5c), much higher than those of Cu foil@Zn||VOH (Figure 5c) and 3D Cu array@Zn||VOH cells (Figure S17b, Supporting Information). The representative discharge–charge curves and the cycling performance of the VOH-based Zn cells at  $2 \text{ A g}^{-1}$  are exhibited in Figure 5d,e, respectively. The Zn@Cu foil||VOH cell delivered an initial discharge capacity of  $241 \text{ mAh g}^{-1}$ , which gradually dropped to  $96 \text{ mAh g}^{-1}$  at the 50th cycle (Figure 5d). This failure was mainly caused by continuous Zn dendrite growth associated with serious side reactions on the Zn@Cu foil anode. When

employing the Zn@3D Cu arrays as anodes, the cycling stability was significantly improved (Figure S18, Supporting Information). The cell using the Zn@Bio-scaffold anode exhibited a high initial discharge capacity of  $295 \text{ mAh g}^{-1}$  with low polarization (Figure 5d), and the capacity retention reached  $\approx 48.2\%$  after 500 cycles with an average CE of  $\approx 99.44\%$  (Figure 5e). The above results were strongly supported by a distribution of relaxation times (DRT) analysis. As shown in the inset of the Figure 5e, peaks related to charge transfer and diffusion responses can be detected at ranges of  $10^{-4}$  to  $10^{-1} \text{ s}$  and  $1$  to  $10^2 \text{ s}$ , respectively (details based on the analysis of Zn||Zn and VOH||VOH symmetrical cells are shown in Figure S19c,d, Supporting Information). It is seen that the integrated area of the charge-transfer peaks (i.e., charge-transfer resistance) of the cells with Zn@Bio-scaffold anode after 50 cycles were much smaller than that of the cell with Zn@Cu foil anode, indicating a decrease of insulating by-products on the

anode|electrolyte interface.<sup>[27]</sup> Meanwhile, the smaller diffusion peak areas of the Zn@Bio-scaffold||VOH cell after cycling compared with those of the Zn@Cu foil||VOH cell implied a shortened ionic-transport distance enabled by the parallel array structure of the Bio-scaffold. The capacity increment and unstable CE at the initial stage were mainly attributed to the activation process of the VOH cathode, which has been reported in previous works.<sup>[37]</sup> In the first few cycles, the VOH cathode undergoes an activation process with the co-insertion of water and protons, which leads to an excess capacity. In the subsequent cycles, a reversible insertion/deintercalation of Zn<sup>2+</sup> ions occurs in the VOH cathode, since the pre-trapped H<sub>2</sub>O acts as an interlayer pillar to stabilize the structure of the VOH cathode.<sup>[38]</sup> This contributes to the following cycles with stable capacity and stable CEs. Such stable anode|electrolyte interface and rapid ionic transport of the Zn@Bio-scaffold

electrode contribute to the significantly enhanced cycling performance as shown in Figure 5e.

The universality of the well-tailored Bio-scaffold for multivalent metal batteries has been further demonstrated in rechargeable nonaqueous Al batteries. The CE of the asymmetric Al cell using Cu foil fluctuated greatly throughout charge–discharge cycling. The voltage profile of this cell presented a low CE of only 49.62% at the 45th cycle (the inset of Figure 6a; the CE of the cell with Bio-scaffold was 99.27% for comparison) and suffered from a rapid battery failure after 50 cycles. The low reversibility of Cu foil in Al batteries can be explained as follows. It is known that Cu metal possesses low metal-philic characteristics for Al.<sup>[39]</sup> The SEM image in Figure 6b presented a heterogeneous and non-planar deposition morphology on the Cu foil, in which plated Al was sparsely distributed on the Cu foil in small “islands” isolated from each

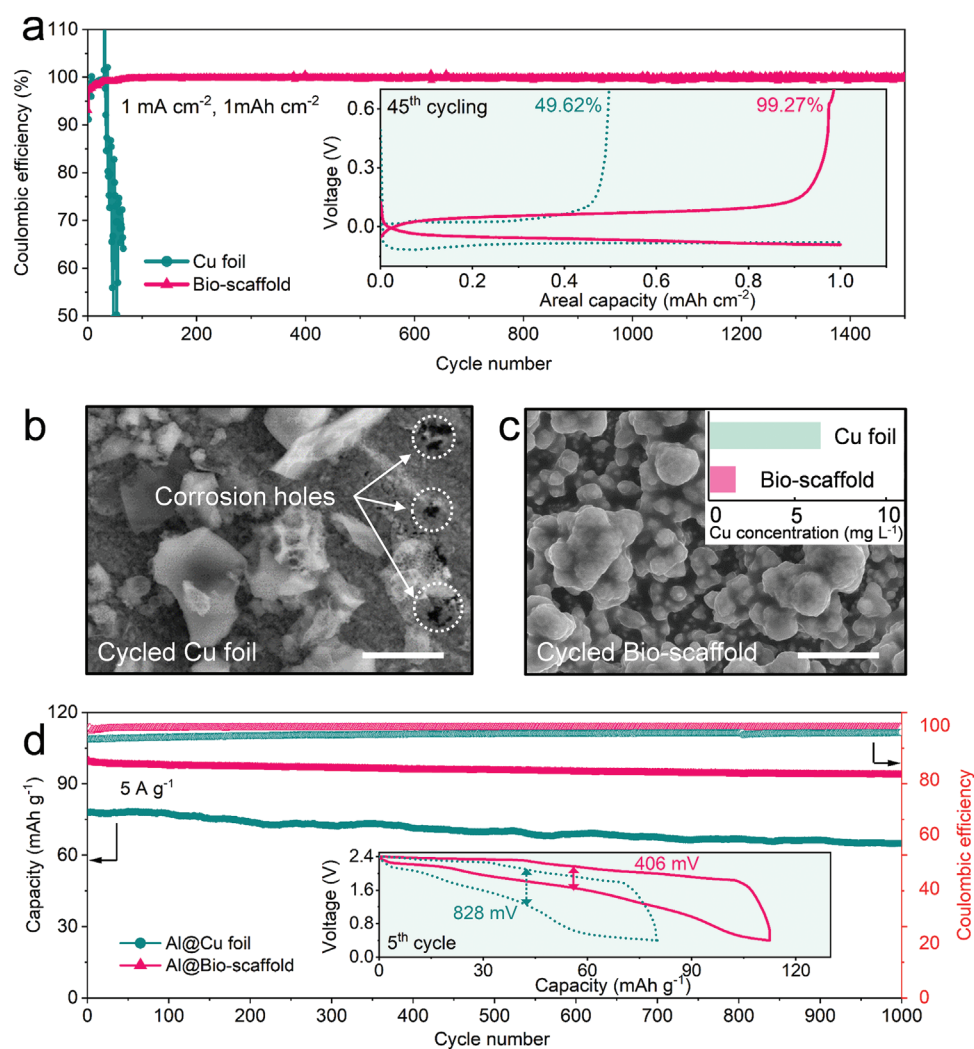


**Figure 6.** Electrochemical performance of Al@Bio-scaffold||graphite batteries. a) CEs of the Al||Cu foil and Al||Bio-scaffold cells at 1 mA cm<sup>-2</sup> with a capacity limit of 1 mAh cm<sup>-2</sup>. Corresponding voltage profiles at the 45th cycle are shown in the inset. b,c) Top-view SEM images of the Al-plated Cu foil (b), and Bio-scaffold (c) disassembled from asymmetric cells after 50 cycles at 1 mA cm<sup>-2</sup>. ICP results of the corresponding Cu concentrations in the electrolyte/seperator after 50 cycles are shown in the inset of (c). d) Cycling performance of Al@Cu foil||graphite and Al@Bio-scaffold||graphite cells at a current density of 5 A g<sup>-1</sup>. Corresponding voltage profiles at the 5th cycle are shown in the inset. Scale bars: 10 μm in (b) and (c).

other. The limited actual contact area between plated Al and Cu substrate seems to trigger sluggish Al plating/stripping kinetics. Besides, it is worth noting that the Cu foil underwent severe corrosion in the presence of chloride-based ionic liquid electrolytes due to the strong corrosivity of chloroaluminate species.<sup>[40]</sup> As can be seen from the SEM image in Figure 6b, massive corrosion holes appeared on the cycled Cu foil surface, meanwhile the Cu concentration in the electrolyte/separator after 50 cycles was as high as 5.46 mg L<sup>-1</sup> based on an inductively coupled plasma (ICP) mass spectroscopy test (see the inset of Figure 6c). Such adverse impacts lead to the low CE of Cu foil in asymmetric Al batteries. The plating/stripping lifespan was prolonged to 480 h for a cell using a 3D Cu array due to the enlarged electrode surface area that alleviates the nuclear barrier to Al plating (Figure S20, Supporting Information). For the cell with the well-tailored Bio-scaffold, Al uniformly plated inside the fractal branches with a relative smooth deposition morphology due to the Al-philic affinity of the CTO-based layer (Figure 6c), meanwhile, the Cu corrosion was efficiently suppressed under the protection of the CTO-based coating layer (see the absence of corrosion holes in Figure 6c and the Cu concentration as low as 1.31 mg L<sup>-1</sup> in the electrolyte/separator after 50 cycles, in the inset of Figure 6c). Consequently, the Al asymmetric cell using Bio-scaffold material displayed high plating/stripping reversibility with an average CE of 99.81% for over 1500 h at 1 mA cm<sup>-2</sup> (Figure 6a).

Al||graphite cells were assembled to assess the feasibility of the Bio-scaffold in Al full batteries. The SEM images of the graphite cathode material are shown in Figure S21 (Supporting Information). The graphite exhibited a morphology as sheet-like particles with an average diameter of 2–5 μm. The specific surface area of natural graphite was measured to be 11.19 m<sup>2</sup> g<sup>-1</sup> using the Brunauer–Emmett–Teller model (Figure S21b, Supporting Information). As demonstrated in Figure 6d, the Al@Bio-scaffold||graphite full cell delivered a high specific capacity of 99.8 mAh g<sup>-1</sup> based on the mass of graphite at 5 A g<sup>-1</sup>, with a high capacity retention of 93.9% for 1000 cycles. In contrast, the Al@Cu foil||graphite full cell suffered from rapid capacity fading with retention of 80.7% for 1000 cycles, mainly originating from the structural deterioration of the Al@Cu foil. The charge/discharge potential gap of the cell using the Al@Cu foil anode (828 mV) was almost twice that of the cell using the Al@Bio-scaffold anode (406 mV, the inset of Figure 6d). The above results confirm the effectiveness of Bio-scaffold for stabilizing Al metal in battery applications.

### 3. Conclusions

Through replicating the architecture of bee hairs, we have developed a versatile Bio-scaffold to support highly efficient multivalent metal plating/stripping. This Bio-scaffold was well-designed through a synergistic utilization of a parallel-aligned array of fractal copper branches paired with a CTO-based coating layer. Confining the Zn and Al metals into this Bio-scaffold, the as-developed composite electrodes exhibited strong resistance against dendrite growth and interfacial side reactions and showed superior performance and stable long-term cycling in Zn and Al full cells. The fractal copper array not only

benefits electrolyte wetting and multivalent ion diffusion, but also effectively reduces local current densities during multivalent metal plating. Meanwhile, the CTO-based coating layer strongly circumvents interfacial side reactions and endows uniform ionic flux. Our key findings pave a new path in the exploration of multivalent metal batteries for low-cost energy storage. Furthermore, the bioinspired scaffold design strategy in this work could be extended to alkali-metal battery applications, including Li-metal batteries and sodium (Na)-metal batteries, thus boosting the prospects for high-efficiency electrochemical energy storage.

### 4. Experimental Section

**Preparation of 3D Cu Array and Bio-Scaffold:** The Bio-scaffold and 3D Cu array were fabricated via a two-step electrochemical deposition process in an electrolytic cell with two Cu plates (99.8%, 20 μm thickness) as the working electrode and counter electrode (Figure S1, Supporting Information).<sup>[41]</sup> The electrolyte was an aqueous solution containing 0.1 M CuSO<sub>4</sub> (99.9%, Sigma Aldrich) and 1.5 M H<sub>2</sub>SO<sub>4</sub> (Sigma Aldrich). A small potential of ≈0.2 V was first applied for 20 s, then an overpotential of ≈1.8 V was subjected to the system for 150 s during the electrochemical deposition process. The as-prepared 3D Cu array as the working electrode was cleaned with deionized water and acetone before use. To prepare the Bio-scaffold, CTO particles were first synthesized by a hydrothermal method.<sup>[42]</sup> 3.4 mL of acetic acid (Sigma Aldrich), 0.34 mL of butyl titanate (Sigma Aldrich), 1 mL of 1 M CaCl<sub>2</sub> (Sigma Aldrich) aqueous solution, 10 mL of 4 g L<sup>-1</sup> poly(vinyl alcohol) (PVA, Sigma Aldrich) aqueous solution and 18 mL of 5 M NaOH (Sigma Aldrich) aqueous solution were mixed under magnetic stirring. The total volume of the solution was kept at 43 mL by adding deionized water. The solution was heated to 200 °C for 6 h in a 50 mL autoclave. Then, the CTO particles were collected by centrifuging the mixture at 10 000 rpm for 10 min, followed by washing with deionized water and drying under 60 °C. The successful synthesis of the CTO was confirmed in Figure S22 (Supporting Information). The Bio-scaffold was prepared by a drop-coating process. 20 mg of CTO particles were dispersed in 20 mL 1 wt% PAN (Mw = 130 000) in *N*-methyl-2-pyrrolidone (NMP, Sigma Aldrich) solution under magnetic stirring. Then, the as-prepared slurry was added dropwise onto the 3D Cu array. Then the coated scaffold was dried under vacuum at 40 °C overnight. The mass loading of the CTO-based layer was 0.1 mg cm<sup>-2</sup>.

**Characterizations:** Transmission electron microscopy (TEM) was accomplished by a Tecnai G2 F30 TEM instrument. SEM and energy-dispersive spectroscopy were obtained using a HITACHI SU8010 FE-SEM. XRD was conducted by a Rigaku D max 2 500 diffractometer with Cu Kα radiation (λ = 1.5418 Å). The SEM images in Figure S15 (Supporting Information), were conducted by ex situ experiments. The cycled substrates were cleaned with deionized water to remove the electrolyte salts, followed by drying under 60 °C before testing. The FT-IR spectra were measured with a Bruker Vertex70 instrument. The water contact angle of the substrate was performed via a contact angle apparatus (KRÜSS DSA30), and the amount of water for one measurement was 4 μL. The specific surface area features of the samples were surveyed by a Nitrogen adsorption-desorption isotherm (ASAP 2020M ± C, Micromeritics). The concentration of Cu ions was measured with ICP (CHNSO, Elementa EL Cube) by immersing the cycled electrolyte/separator in 20 mL FeCl<sub>3</sub> aqueous solution for 24 h. In situ optical observations were carried out to visualize Zn plating/stripping behavior on different substrates by adopting a polytetrafluoroethylene cell with a transparent quartz window (Kejing, STC-Q), in which a specified fresh substrate and Zn foil (100 μm) were employed as the working electrode and counter electrode with a separation distance of ≈2.5 mm, respectively. The effective geometric area for Zn plating/stripping on different substrates was 1 cm<sup>2</sup>. The applied current density was set at

5 mA cm<sup>-2</sup> by using an electrochemical working station (NEWARE), while a digital camera (Sony NEX6) was used to capture photographs with a capture interval time of 30 s during the Zn plating/stripping processes. The LSV and CA measurements were conducted on a Biologic VMP-3 electrochemical station (Bio-Logic Science Instruments, France) with a three-electrode configuration using a platinum (Pt) plate as the counter electrode, and an Ag/AgCl electrode as the reference electrode. 1 M NaSO<sub>4</sub> aqueous solution was used as the electrolyte in the LSV test, while 2 M ZnSO<sub>4</sub> aqueous solution was used as the electrolyte in the CA test.

**Assembly and Testing of Zn and Al Batteries:** The electrochemical performance was measured via CR2032 coin cells and Swagelok cells. For coin cells, Zn foil, Cu foil, 3D Cu array, and Bio-scaffold were cut into disk-shaped electrodes with a diameter of 12 mm. Glass fiber membranes with a diameter of 19 mm (Whatman, GF/D) were used as the separator. CE measurements were carried out on Zn||Cu asymmetrical cells. Cu foil, 3D Cu array, and Bio-scaffold were used as the working electrodes, while Zn foil was applied as the counter electrode. The Zn plating/stripping tests were performed on Zn||Zn symmetrical cells. Zn foil, Cu foil@Zn, 3D Cu array@Zn, and Bio-scaffold@Zn were used as working and counter electrodes in each cell. The Cu foil@Zn was prepared by electrochemical deposition with Cu foil as the working electrode and Zn plate as the counter electrode and reference electrode. Typically, 30 g of ZnSO<sub>4</sub>·7H<sub>2</sub>O (Sigma Aldrich), 30 g of Na<sub>2</sub>SO<sub>4</sub> (Sigma Aldrich), and 5 g of H<sub>3</sub>BO<sub>3</sub> (Sigma Aldrich) were dissolved in 200 mL of deionized water as electrolyte, and the electrodeposition was conducted under a current of 12 mA cm<sup>-2</sup> for 50 min (capacity: 6 mAh cm<sup>-2</sup>). 3D Cu array@Zn and Bio-scaffold@Zn were prepared using the same procedures. 2 M ZnSO<sub>4</sub> aqueous solution was used in both Zn||Cu and Zn||Zn cells as electrolytes.

For Zn||VOH full cells, CR2032 coin cells were assembled using VOH as the cathode, glass fiber membrane as the separator, 2 M ZnSO<sub>4</sub> aqueous solution as the electrolytes, and different as-prepared electrodes (Cu foil@Zn, 3D Cu array@Zn, and Bio-scaffold@Zn) as the anode. The VOH was prepared by reducing V<sub>2</sub>O<sub>5</sub> using a hydrothermal method.<sup>[37b]</sup> 1 g V<sub>2</sub>O<sub>5</sub> (Sigma Aldrich) and 1 g sucrose (Sigma Aldrich) were mixed with 70 mL deionized water under magnetic stirring. Then the mixed solution was transformed into an autoclave and heated at 100 °C for 12 h. After the hydrothermal reaction, the VOH powders were collected by filtration and washed with deionized water and ethanol. The VOH powders were dried at 60 °C in an oven for 12 h. Then, the VOH cathode was fabricated by mixing 70 wt% VOH powder, 20 wt% super P, and 10 wt% polyvinylidene fluoride (PVDF, Macklin) in NMP to form a slurry, and then coated onto stainless steel foils. Electrochemical impedance spectroscopy was implemented using a Biologic VMP-3 electrochemical workstation within the range of 10<sup>5</sup> to 10<sup>-2</sup> Hz and an amplitude of 10 mV. The DRT analysis was performed by using DRT Tools.<sup>[43]</sup> CVs of the Zn||VOH full cells were carried out on the Biologic VMP-3 electrochemical workstation at 0.5–1.5 V with a scanning rate of 0.1 mV s<sup>-1</sup>. The GITTs were measured at a 0.1 A g<sup>-1</sup> pulse current for 5 min and relaxed for 60 min. The Zn||VOH full cells were cycled in a voltage window of 0.5–1.5 V at various rates.

Swagelok cells with molybdenum current collectors and glass fiber separators were assembled for Al cells. The electrolyte was prepared by mixing (EMIm)Cl (1-ethyl-3-methylimidazolium chloride, Sigma Aldrich, 98%) and AlCl<sub>3</sub> (Sigma Aldrich) with a molar ratio of 1:1.3. CE measurements were carried out on Al||Cu asymmetrical cells. For Al||graphite full cells, the anode was prepared by electrochemical deposition in Al||Cu configurations under a current of 5 mA cm<sup>-2</sup> for 1 h (capacity: 5 mAh cm<sup>-2</sup>). The graphite cathode was fabricated by mixing 70 wt% graphite powders (Aladdin), 20 wt% super P, and 10 wt% PVDF in NMP to form a slurry, and then coated onto molybdenum foils. The Al||graphite full cells were cycled between 0.5 and 2.4 V at 5 A g<sup>-1</sup> to measure the cycling performance on a NEWARE battery-testing system.

**Computations:** Two-dimension discrete models of the electric field at the interface between different anodes and electrolytes were built to clarify the effect of the 3D structure of the host with a high dielectric constant ( $\epsilon$ ) on the plating process. To simulate the electrical field ( $-\nabla\psi$ ) on Cu foil, 3D Cu array, and Bio-scaffold, the Poisson equation

$\nabla(\epsilon_0\epsilon_r\nabla\psi) = 0$  was solved based on COMSOL Multiphysics. The boundary condition was as follows: the cathodic potential was set as 1 V (experimentally determined by discharge voltage plateau), while the anodic potential was set as 0 V.<sup>[29]</sup>

The theoretical calculations of the binding energies were performed with the Vienna ab initio Simulation Package based on the DFT. The Projector-augmented wave was used for the electron-ion interactions and generalized gradient approximation functional of Perdew, Burke, and Enzerhof were employed to evaluate the exchange-correlation energy. The D-3 corrections of Grimme were used to calculate the interactions between the Zn atom and the substrates. The cut-off energy is set to be 400 eV with  $8 \times 8 \times 1$  gamma-centered k points. The energy convergence tolerance was set to below  $1 \times 10^{-6}$  eV atom<sup>-1</sup> in geometry optimization and  $1 \times 10^{-8}$  eV atom<sup>-1</sup> for single point energy. To avoid the interaction between cells in space, the vacuum layer was set as 15 Å. The surface binding energy was calculated with the following equation:  $\Delta E = E_{\text{total}} - E_{\text{surf}} - E_{\text{Zn}}$ , where  $E_{\text{total}}$ ,  $E_{\text{surf}}$ , and  $E_{\text{Zn}}$  represent the total energy after the combination of different models with a Zn atom; the energy after the optimization of Zn, Cu, and CTO structure; and the energy of a Zn atom, respectively.

## Supporting Information

Supporting Information is available from the Wiley Online Library or from the author.

## Acknowledgements

B.L. would like to acknowledge the support funded by the National Nature Science Foundation of China (No. 51872157), Shenzhen Key Laboratory (ZDSYS201707271615073), and Guangdong Technical Plan Project (No. 2017B090907005). G.W. would like to acknowledge the support from the Australian Research Council (ARC) Discovery Projects (DP200101249 and DP210101389) and the ARC Research Hub for Integrated Energy Storage Solutions (IH180100020).

Open access publishing facilitated by University of Technology Sydney, as part of the Wiley - University of Technology Sydney agreement via the Council of Australian University Librarians.

## Conflict of Interest

The authors declare no conflict of interest.

## Data Availability Statement

The data that support the findings of this study are available from the corresponding author upon reasonable request.

## Keywords

biomimetic scaffolds, dendrite growth, fractal structures, interfacial side reactions, multivalent metal batteries

Received: August 1, 2022

Revised: September 2, 2022

Published online: October 17, 2022

[1] M. Li, J. Lu, Z. Chen, K. Amine, *Adv. Mater.* **2018**, *30*, 1800561.

- [2] a) Z. Liu, Y. Huang, Y. Huang, Q. Yang, X. Li, Z. Huang, C. Zhi, *Chem. Soc. Rev.* **2020**, 49, 180; b) J. W. Choi, D. Aurbach, *Nat. Rev. Mater.* **2016**, 1, 16013.
- [3] a) X. Tang, D. Zhou, B. Zhang, S. Wang, P. Li, H. Liu, X. Guo, P. Jaumaux, X. Gao, Y. Fu, C. Wang, C. Wang, G. Wang, *Nat. Commun.* **2021**, 12, 2857; b) Y. Tian, G. Zeng, A. Rutt, T. Shi, H. Kim, J. Wang, J. Koettgen, Y. Sun, B. Ouyang, T. Chen, Z. Lun, Z. Rong, K. Persson, G. Ceder, *Chem. Rev.* **2021**, 121, 1623.
- [4] a) Y. Liang, H. Dong, D. Aurbach, Y. Yao, *Nat. Energy* **2020**, 5, 646; b) H. Wang, M. Wang, Y. Tang, *Energy Storage Mater.* **2018**, 13, 1.
- [5] V. Verma, S. Kumar, W. Manalastas, R. Satish, M. Srinivasan, *Adv. Sustainable Syst.* **2019**, 3, 1800111.
- [6] M.-C. Lin, M. Gong, B. Lu, Y. Wu, D.-Y. Wang, M. Guan, M. Angell, C. Chen, J. Yang, B.-J. Hwang, H. Dai, *Nature* **2015**, 520, 324.
- [7] B.-F. Cui, X.-P. Han, W.-B. Hu, *Small Struct.* **2021**, 2, 2000128.
- [8] L. Yuan, J. Hao, C.-C. Kao, C. Wu, H.-K. Liu, S.-X. Dou, S.-Z. Qiao, *Energy Environ. Sci.* **2021**, 14, 5669.
- [9] O. M. Leung, T. Schoetz, T. Prodromakis, C. Ponce de Leon, *J. Electrochem. Soc.* **2021**, 168, 056509.
- [10] Z. Hou, Y. Gao, R. Zhou, B. Zhang, *Adv. Funct. Mater.* **2021**, 32, 2107584.
- [11] a) H. Lv, S. Yang, C. Li, C. Han, Y. Tang, X. Li, W. Wang, H. Li, C. Zhi, *Energy Storage Mater.* **2021**, 39, 412; b) Y. Wang, L. Zhang, F. Zhang, X. Ding, K. Shin, Y. Tang, *J. Energy Chem.* **2021**, 58, 602.
- [12] L. Suo, O. Borodin, T. Gao, M. Olguin, J. Ho, X. Fan, C. Luo, C. Wang, K. Xu, *Science* **2015**, 350, 938.
- [13] Q. Li, D. Wang, B. Yan, Y. Zhao, J. Fan, C. Zhi, *Angew. Chem., Int. Ed.* **2022**, 61, e202202780.
- [14] J. Shin, J. Lee, Y. Kim, Y. Park, M. Kim, J. W. Choi, *Adv. Energy Mater.* **2021**, 11, 2100676.
- [15] R. Yuksel, O. Buyukcakir, W. K. Seong, R. S. Ruoff, *Adv. Energy Mater.* **2020**, 10, 1904215.
- [16] Z. Guo, L. Fan, C. Zhao, A. Chen, N. Liu, Y. Zhang, N. Zhang, *Adv. Mater.* **2022**, 34, 2105133.
- [17] J. Zheng, D. C. Bock, T. Tang, Q. Zhao, J. Yin, K. R. Tallman, G. Wheeler, X. Liu, Y. Deng, S. Jin, A. C. Marschillok, E. S. Takeuchi, K. J. Takeuchi, L. A. Archer, *Nat. Energy* **2021**, 6, 398.
- [18] a) X. Li, Q. Li, Y. Hou, Q. Yang, Z. Chen, Z. Huang, G. Liang, Y. Zhao, L. Ma, M. Li, Q. Huang, C. Zhi, *ACS Nano* **2021**, 15, 14631; b) X. Tang, D. Zhou, P. Li, X. Guo, B. Sun, H. Liu, K. Yan, Y. Gogotsi, G. Wang, *Adv. Mater.* **2020**, 32, 1906739.
- [19] Z. Kang, C. Wu, L. Dong, W. Liu, J. Mou, J. Zhang, Z. Chang, B. Jiang, G. Wang, F. Kang, C. Xu, *ACS Sustainable Chem. Eng.* **2019**, 7, 3364.
- [20] C. Li, X. Shi, S. Liang, X. Ma, M. Han, X. Wu, J. Zhou, *Chem. Eng. J.* **2020**, 379, 122248.
- [21] H. Chen, A. Pei, J. Wan, D. Lin, R. Vilá, H. Wang, D. Mackanic, H.-G. Steinrück, W. Huang, Y. Li, A. Yang, J. Xie, Y. Wu, H. Wang, Y. Cui, *Joule* **2020**, 4, 938.
- [22] K. A. Khan, T. Liu, *Insects* **2022**, 13, 189.
- [23] a) T. Young, *Philos. Trans. R. Soc. London* **1805**, 95, 65; b) R. N. Wenzel, *Ind. Eng. Chem.* **1936**, 28, 988.
- [24] L. Wen, Y. Tian, L. Jiang, *Angew. Chem., Int. Ed.* **2015**, 54, 3387.
- [25] J. Cao, D. Zhang, X. Zhang, Z. Zeng, J. Qin, Y. Huang, *Energy Environ. Sci.* **2022**, 15, 499.
- [26] S. H. Park, S. Y. Byeon, J.-H. Park, C. Kim, *ACS Energy Lett.* **2021**, 6, 3078.
- [27] J. Ding, Y. Liu, S. Huang, X. Wang, J. Yang, L. Wang, M. Xue, X. Zhang, J. Chen, *ACS Appl. Mater. Interfaces* **2021**, 13, 29746.
- [28] J. Cong, X. Shen, Z. Wen, X. Wang, L. Peng, J. Zeng, J. Zhao, *Energy Storage Mater.* **2021**, 35, 586.
- [29] S. Zhou, Y. Wang, H. Lu, Y. Zhang, C. Fu, I. Usman, Z. Liu, M. Feng, G. Fang, X. Cao, S. Liang, A. Pan, *Adv. Funct. Mater.* **2021**, 31, 2104361.
- [30] Z. Zhao, J. Zhao, Z. Hu, J. Li, J. Li, Y. Zhang, C. Wang, G. Cui, *Energy Environ. Sci.* **2019**, 12, 1938.
- [31] W. Zhang, H. L. Zhuang, L. Fan, L. Gao, Y. Lu, *Sci. Adv.* **2018**, 4, aar4410.
- [32] V. V. Lemanov, A. V. Sotnikov, E. P. Smirnova, M. Weihnacht, R. Kunze, *Solid State Commun.* **1999**, 110, 611.
- [33] Q. Li, A. Chen, D. Wang, Z. Pei, C. Zhi, *Joule* **2022**, 6, 273.
- [34] X. Xu, K. Lin, D. Zhou, Q. Liu, X. Qin, S. Wang, S. He, F. Kang, B. Li, G. Wang, *Chem* **2020**, 6, 902.
- [35] M. Yan, P. He, Y. Chen, S. Wang, Q. Wei, K. Zhao, X. Xu, Q. An, Y. Shuang, Y. Shao, K. T. Mueller, L. Mai, J. Liu, J. Yang, *Adv. Mater.* **2018**, 30, 1703725.
- [36] M. Yan, N. Dong, X. Zhao, Y. Sun, H. Pan, *ACS Energy Lett.* **2021**, 6, 3236.
- [37] a) Y. Kim, Y. Park, M. Kim, J. Lee, K. J. Kim, J. W. Choi, *Nat. Commun.* **2022**, 13, 2371; b) W. Liu, L. Dong, B. Jiang, Y. Huang, X. Wang, C. Xu, Z. Kang, J. Mou, F. Kang, *Electrochim. Acta* **2019**, 320, 134565; c) X. Zeng, K. Xie, S. Liu, S. Zhang, J. Hao, J. Liu, W. K. Pang, J. Liu, P. Rao, Q. Wang, J. Mao, Z. Guo, *Energy Environ. Sci.* **2021**, 14, 5947.
- [38] R. Li, H. Zhang, Q. Zheng, X. Li, *J. Mater. Chem. A* **2020**, 8, 5186.
- [39] Q. Zhao, J. Zheng, Y. Deng, L. Archer, *J. Mater. Chem. A* **2020**, 8, 23231.
- [40] Y. Zhang, S. Liu, Y. Ji, J. Ma, H. Yu, *Adv. Mater.* **2018**, 30, 1706310.
- [41] D. Wakerley, S. Lamaison, F. Ozanam, N. Menguy, D. Mercier, P. Marcus, M. Fontecave, V. Mougél, *Nat. Mater.* **2019**, 18, 1222.
- [42] L. Fan, W. Peng, J. Meng, *Inorg. Chem. Ind.* **2011**, 43, 16.
- [43] T. H. Wan, M. Saccoccio, C. Chen, F. Ciucci, *Electrochim. Acta* **2015**, 184, 483.